Title

Permeability Variations Associated With Fault Reactivation in a Claystone Formation Investigated by Field Experiments and Numerical Simulations

Journal

Journal of Geophysical Research: Solid Earth, 123(2)

ISSN

2169-9313

Authors

Jeanne, Pierre

Guglielmi, Yves

Rutqvist, Jonny

et al.

Publication Date

2018-02-01

DOI

10.1002/2017jb015149

Peer reviewed

AGU PUBLICATIONS

JGR

Journal of Geophysical Research: Solid Earth

RESEARCH ARTICLE
10.1002/2017JB015149

Key Points:
- Rate-and-state permeability law allows reproducing the complex fault behavior at rupture
- Ruptures can create or destroy permeability
- Only "intermediate" diffusivity led to secondary rupture associated with fluid diffusion

Supporting Information:
- Supporting Information S1
- Table S1

Correspondence to:
P. Jeanne,
pjeanne@lbl.gov

Citation:
Jeanne, P., Guglielmi, Y., Rutqvist, J., Nussbaum, C., & Birkholzer, J. (2018). Permeability variations associated with fault reactivation in a claystone formation investigated by field experiments and numerical simulations. *Journal of Geophysical Research: Solid Earth*, *123*. https://doi.org/10.1002/2017JB015149

Received 23 OCT 2017
Accepted 6 FEB 2018
Accepted article online 13 FEB 2018

Permeability Variations Associated With Fault Reactivation in a Claystone Formation Investigated by Field Experiments and Numerical Simulations

Pierre Jeanne[1], Yves Guglielmi[1], Jonny Rutqvist[1], Christophe Nussbaum[2], and Jens Birkholzer[1]

[1]Lawrence Berkeley National Laboratory, Energy Geoscience Division, Berkeley, CA, USA, [2]Federal Office of Topography, Swisstopo, Wabern, Switzerland

Abstract We studied the relation between rupture and changes in permeability within a fault zone intersecting the Opalinus Clay formation at 300 m depth in the Mont Terri Underground Research Laboratory (Switzerland). A series of water injection experiments were performed in a borehole straddle interval set within the damage zone of the main fault. A three-component displacement sensor allowed an estimation of the displacement of a minor fault plane reactivated during a succession of step rate pressure tests. The experiment reveals that the fault hydromechanical (HM) behavior is different from one test to the other with varying pressure levels needed to trigger rupture and different slip behavior under similar pressure conditions. Numerical simulations were performed to better understand the reason for such different behavior and to investigate the relation between rupture nucleation, permeability change, pressure diffusion, and rupture propagation. Our main findings are as follows: (i) a rate frictional law and a rate-and-state permeability law can reproduce the first test, but it appears that the rate constitutive parameters must be pressure dependent to reproduce the complex HM behavior observed during the successive injection tests; (ii) almost similar ruptures can create or destroy the fluid diffusion pathways; (iii) a too high or too low diffusivity created by the main rupture prevents secondary rupture events from occurring whereas "intermediate" diffusivity favors the nucleation of a secondary rupture associated with the fluid diffusion. However, because rupture may in certain cases destroy permeability, this succession of ruptures may not necessarily create a continuous hydraulic pathway.

1. Introduction

It is well known that industrial scale injection of fluids into the subsurface can generate large overpressures perturbing effective stress, which could potentially induce shear rupture along preexisting faults. How the rupture and associated slip will evolve (seismic or aseismic) and how the hydraulic properties will be affected (enhancement or destruction of permeability) is not well understood. These questions have become an important topic of discussion especially in North America and Europe where induced seismic events have been felt by, and unsettled, local communities (e.g., Jones, Oklahoma; Hand, 2014), caused damage to ground-surface structures (e.g., Basel, Switzerland; Giardini, 2009), resulted in large losses for property owners (e.g., Loppersum, Netherlands; Tagliabue, 2013), and led to litigation over compensation for damage. It is also desirable, if at all possible, to characterize changes in permeability associated with seismic events. An increase in permeability along a reactivated fault could be economically beneficial (e.g., providing permeability for Enhanced Geothermal Systems in hot dry rocks; Jeanne et al., 2014) or environmentally problematic (e.g., creating a flow path for upward fluid leakage and possible contamination of shallow potable groundwater resources in case of a CO_2 sequestration project; Zoback & Gorelick, 2012).

Our current understanding of fault stability and changes in hydraulic properties comes mainly from experimental laboratory studies. When a tangential shearing stress (τ) is applied parallel to a discontinuity in a rock sample subject to a normal load (σ_n), this force must reach some critical value in order for sliding to occur (Amontons, 1699). The fluid pressure (P_f) can also facilitate the slip by reducing the effective normal load (Terzaghi, 1923). The relation between τ, σ_n, and P_f is known as the Mohr-Coulomb law (Coulomb, 1773; Hubbert & Rubey, 1959) and may be written as

$$\tau = \mu_s \times (\sigma_n - P_f) \quad (1)$$

with μ_s the coefficient of static friction. Once sliding is initiated, two effects seem to act on the coefficient of

friction. First, there is a "rate" effect, the friction coefficient increasing or decreasing with the sliding velocity (V). Following the rate effect, there is a "state" effect that corresponds to an evolution of the friction coefficient over time. Friction is found to evolve to a new steady-state value over a characteristic slip distance (D_c; Dieterich, 1978; Rabinowicz, 1958). D_c is interpreted as a memory distance over which the contact population between the sliding surface walls changes (Dieterich, 1978, 1979; Ruina, 1983). These observations led to the definition of the coefficient of dynamic friction, μ_d, and to the development of the so-called "rate-and-state" dependent friction (Ruina, 1983) described by the following empirical constitutive law:

$$\mu = \mu_0 + a \ln\left(\frac{V}{V_0}\right) + b \ln\left(\frac{V_0\theta}{D_c}\right) \tag{2}$$

where μ_0 is the initial friction coefficient (in this model the distinction between μ_s and μ_d disappears), V_0 is the initial sliding velocity, and a and b are two dimensionless constants that reflect the rate at which the friction coefficient varies with changes in ln$V$ and θ. θ is the state variable, and it has a unit of time and represents the average age of the asperity contacts. According to Ruina (1983), θ varies as

$$\frac{d\theta}{dt} = 1 - \frac{V\theta}{D_c} \tag{3}$$

Steady state is reached after a long period of time when dθ/dt tends to zero. In this case,

$$\theta_{ss} = D_c/V \tag{4}$$

and the evolution law equation (3) can be written as equation (5) and equation (2) as equation (6):

$$\frac{d\theta}{dt} = -\frac{V}{D_c}\,(\theta - \theta_{ss}) \tag{5}$$

$$\mu = \mu_0 + (a-b)\ln\frac{V}{V_0} \tag{6}$$

The rate-and-state friction theory is used to quantify the stability regime at the interface of two elastic bodies in contact (Marone, 1998). It does not consider any dilatancy or compaction effect of the porosity that are phenomena observed both at the laboratory and reservoir scales (Pine & Batchelor, 1984; Segall & Rice, 1995). Despite this simplification, field experiments (Guglielmi, Cappa, et al., 2015) and aftershock studies (Carpenter et al., 2014; Sleep & Blanpied, 1992; Townend & Zoback, 2001) suggest that the rate-and-state friction physics can be scaled to describe the stability of natural fractures and faults. If $a - b > 0$, the material is said to be velocity strengthening favoring stable sliding. Inversely, if $a - b < 0$, the material is said to be velocity weakening (Scholz, 1998), and earthquake slip may occur. Moreover, Scruderi and Collettini (2016) recently showed that the friction constitutive parameters ($a - b$) and the critical slip distance D_c vary with fluid pressure.

For the sake of simplicity, a strain-weakening friction law has been adopted in geomechanical simulations to represent fault stability and to simulate a brittle (slip weakening) fault rheology (Rutqvist et al., 2016). In this case, the coefficient of static friction μ_s drops linearly to a residual coefficient of dynamic friction, μ_d, when the plastic shear strain reaches a critical value.

How the permeability (k) along a fault is evolving during and after a slip event is also a key question. Numerous laboratory experiments on rough fractures performed since the 1980s have shown that once a fracture is sheared, it would likely remain open because of fracture self-propping (due to surface roughness) increasing its permeability (Rutqvist & Stephansson, 2003). However, while most of those experiments were conducted with hard crystalline rock samples related to nuclear waste disposal research, other experiments on softer rocks, such as shale, have shown that permeability might increase or decrease with shear depending on the stress normal to the fractures (Gutierrez et al., 2000).

In this paper, we investigate the coupling between fault slip and permeability by analyzing a water injection test performed in a fault zone intersecting the Opalinus Clay formation at 300 m depth in the Mont Terri Underground Research Laboratory, Switzerland. A three-component displacement sensor, clamped on the walls of a borehole section that was hydraulically isolated by inflatable packers on each side, was set within the damage zone of the fault. Fault movements were monitored synchronously with fluid pressure variations triggered by controlled fluid injections. Numerical simulations were performed to reproduce these

experiments in order to better understand (i) the relation between slip and changes in permeability and (ii) the mechanisms leading to induced seismicity.

2. Fault Permeability Model Linked With Rate and State Friction

A number of models for changes in fracture permeability with stress and deformations can be found in the literature (Rutqvist & Stephansson, 2003). A simple one would be to consider that the permeability is enhanced by a fixed factor when rupture occurs (equation ((7)); Rinaldi et al., 2015; Guglielmi, Elsworth, et al., 2015; Permeability Law 1).

$$k_{hm} = k_{ini} \times \text{Factor} \tag{7}$$

A more complex permeability law previously applied to fault activation in Rinaldi et al. (2014) describes the permeability evolution in response to deformation in a transversely isotropic permeable medium considering a single fracture set oriented parallel to the fault. This law suggests that the permeability depends on the effective normal stress (σ'_n) and on the plastic shear (e_{pss}) and tensile strain (e_{pts}; equation (8); Hsiung et al. 2005; Permeability Law 2).

$$\begin{cases} \kappa_{hm} = \kappa_0 \left[\dfrac{a}{c\left(c\sigma'_n + 1\right)} \sqrt{\dfrac{\phi_0}{12\kappa_0}} + \dfrac{e_{pts} + e_{pss} \tan\psi}{\phi_0} \right]^3 \\ a = K^{-1} \\ c = \dfrac{-1 \pm \sqrt{1 + 4\sigma'_n a \sqrt{\dfrac{\phi_0}{12\kappa_0}}}}{2\sigma'_{n0}} \end{cases} \tag{8}$$

where a and c are two empirical constants for describing the fracture normal closure versus stress hyperbola (Bandis et al., 1983) that can be approximated from the limiting fracture normal stiffness (K) at zero effective normal stress and from the initial normal effective stress (σ'_{n0}). The last term in equation (8) is equivalent to irreversible porosity changes induced by shear and tensile rupture according to

$$\begin{cases} \phi_{hm} = \phi_0 + \Delta\phi_{fp} \\ \Delta\phi_{fp} = e_{pts} + e_{pss} \tan\psi \end{cases} \tag{9}$$

where $\Delta\phi_{fp}$ is the changes in fracture porosity that depend on plastic tensile strain (e_{pts}) and plastic shear strain (e_{pss}). ψ represents the dilation angle of reactivated fractures.

Finally, Marone et al. (1990) based on laboratory studies postulate that the porosity (ϕ) of a fault gouge can compact or dilate during a slip event. Segall and Rice (1995) linked these observations and measurements to the rate and state theory and postulated that the porosity (ϕ) of a fault gouge is a function of state, and so based on equation (4), Segall and Rice (1995) proposed equation (10) where porosity is indirectly rate dependent:

$$\phi_{hm} = \phi_0 - \varepsilon \ln(V_0\theta / D_c) \tag{10}$$

where ϕ_0 is the initial porosity and ε is a dilatancy coefficient.

Here we link the porosity to the permeability using equation (10) (modified from Hsiung et al., 2005; Permeability Law 3).

$$\begin{cases} \kappa_{hm} = \kappa_0 \left[\dfrac{a}{c\left(c\sigma'_n + 1\right)} \sqrt{\dfrac{\phi_0}{12\kappa_0}} + \dfrac{\phi_{hm} - \phi_0}{\phi_0} \right]^3 \\ a = K^{-1} \\ c = \dfrac{-1 + \sqrt{1 + 4\sigma'_{n0} a \sqrt{\dfrac{\phi_0}{12\kappa_0}}}}{2\sigma'_{n0}} \end{cases} \tag{11}$$

This equation accounts for permeability variations due to dilation or compaction of fault porosity associated with slip velocity and with changes in the effective normal stress (σ'_n).

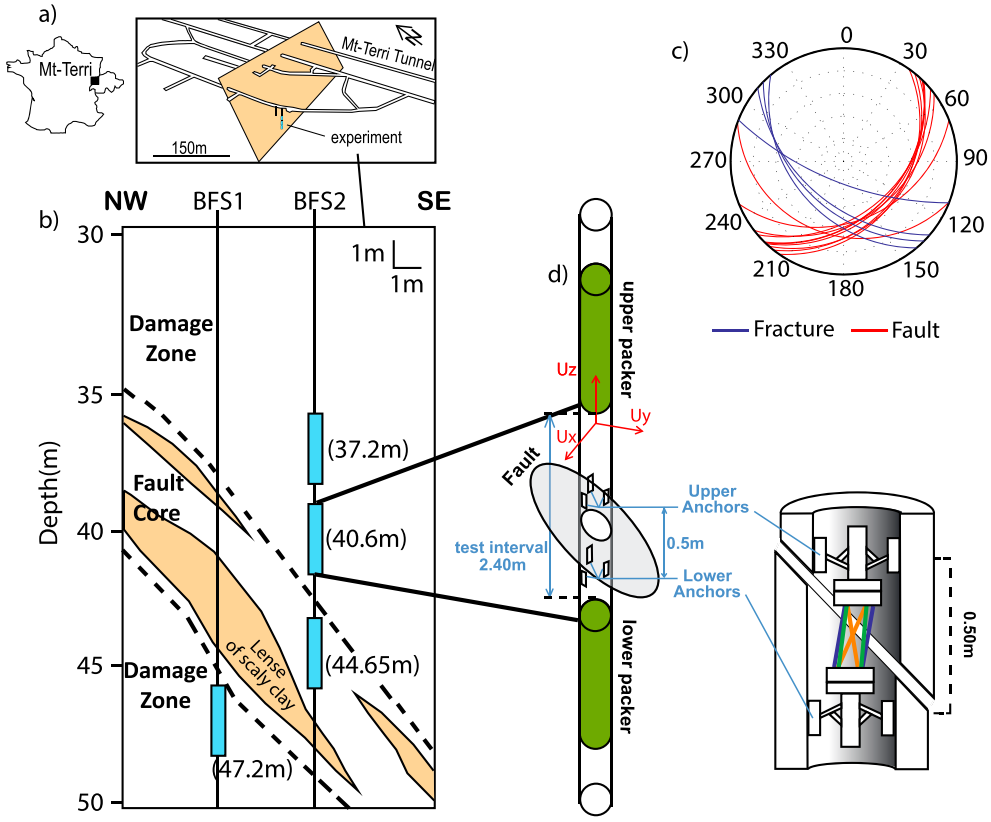

Figure 1. (a) Location of the study area. (b) Schematic cross section of the fault zone showing the packed-off sections in blue. (c) Stereographic projections (lower hemisphere) in the packed-off sections at 40.6 m. (d) HPPP test equipment setup and schematic view of the three-dimensional deformation unit. Tubes are differently colored to show that they display different deformations when there is a relative movement of the rings anchored to the borehole wall across the activated fracture.

3. Field Experiment

The injection experiment analyzed in this article was conducted in the damage zone of the main fault intersecting the Mont Terri rock laboratory in Switzerland (Figure 1a). Injections occurred in a vertical borehole (BFS2) about 40.6 m below the floor of one of the drifts of rock lab. At this location, the 40SE striking fault dips N050°. Water was injected into a 2.4 m long chamber between two inflatable packers spanning four fractures (with strike N110° to N140° and dipping 25° to 45°SW) and 10 fault planes (nine with strike N035° to N068° and dipping 31° to 40°SE; and one with strike N110° and dipping 24°SW; Figures 1b and 1c). While pressurizing the interval, we used a High Pulse Poroelasticity Probe (HPPP; Guglielmi et al., 2013; Figure 1c) to simultaneously monitor the three-dimensional displacement of the injection chamber wall, the fluid pressure variation, and the flow rate at a 500 Hz sampling rate. The accuracy on the measured displacements and pressure are ±5 μm and ±0.001 MPa, respectively. The three-dimensional displacement of the injection chamber wall is monitored by a three-component extensometer centered along the axis connecting the two packers in the injection chamber (Figure 1d). This extensometer is fixed to the borehole wall by hydraulically operated anchors. Six small-diameter and deformable steel tubes connect two rings with varying orientations—making a cylindrical cage linking the upper and lower rings. Extension and torsion between the rings is resolved from the inversion of the deformations of the six tubes. The cage used in this experiment is 0.5 m long and 0.1 m diameter (Figure 1d). Tube deformations are captured with six fiber optic Bragg gratings that are attached to each tube and distributed along one single continuous fiber that brings the sensor signals to the surface-mounted data acquisition system. An inversion algorithm is used to calculate the relative three-dimensional displacements (*x*, *y*, and *z* respectively oriented north, west, and vertical) of the center of the upper ring toward the center of the lower ring from the tube deformations that are continuously monitored during the test.

Tests start with a first step rate test (SRT1) where the pressure is increased step by step with a manual pump to minimize the potential injected volume in the formation when failure is occurring. SRT1 is performed to

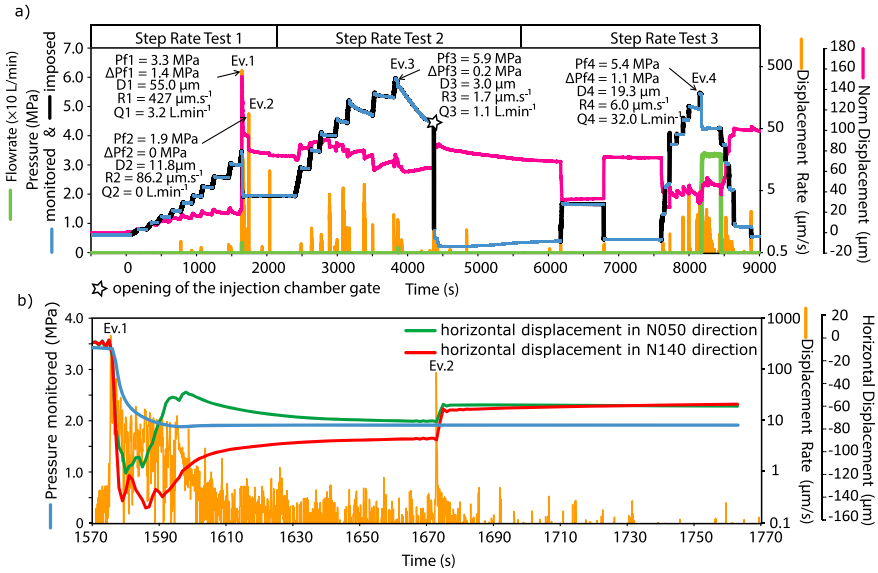

Figure 2. Evolution of (a) the imposed (black curve) and monitored (blue curve) pressure, the norm of the relative displacement vector of the borehole wall (purple curve), the displacement rate (orange curve), and the flow rate (green) during SRT1, SRT2, and SRT3. (b) Zoom on the evolution of the monitored pressure (blue curve), the relative horizontal displacements (green and red curves), and the displacement rate (orange curve) monitored at the end of SRT1.

characterize the stress and the initial hydraulic and mechanical properties of the fault. This test is repeated a second time (SRT2). Then, the same protocol is applied using an engine pump (SRT3) in order to inject larger volumes into the formation when failure is occurring to explore the role of hydromechanical (HM) effects within the fractures reactivated farther away from the injection point.

STR1 ended when the injected pressure reached 3.3 MPa (P_{f1}), triggering a large 55 µm displacement with a maximum displacement rate of 427 µm s^{-1}. This first event (Ev.1) is associated with a 1.4 MPa pressure drop and a small increase in flow rate up to 3.2 L min^{-1} (Figure 2a). This event is followed by a period of 750 s, without any flow rate or changes in fluid pressure within the injection chamber. However, just after Ev.1, small displacements with displacement rates ≈18 µm s^{-1} were monitored during ≈130 s ending by a second event (Ev.2). Ev.2 is characterized by a large 11.8 µm displacement with a maximum displacement rate of 86 µm s^{-1} (Figure 2a).

During SRT2, the fluid pressure was increased up to a maximum pressure twice of 6.0 MPa (two times larger than P_{f1}), but only small displacements (≈3.0 µm) were triggered. These events started occurring once the injected fluid pressure exceeded P_{f1}. Their displacement rates range from 1.7 to 6.0 µm s^{-1}. No pressure drop and no increase in flow rate are associated with them expect for one event (Ev.3) occurring at 5.9 MPa and causing a 0.2 MPa pressure drop associated with a small increase in flow rate up to 1.1 L min^{-1}.

Then a third step rate test (STR3) was performed with the engine pump. In this test, a 19.3 µm displacement was triggered at an injected pressure of 5.3 MPa with a displacement rate of 6.0 µm s^{-1}. This event (Ev.4) is associated with a large 32 L min^{-1} increase in flow rate. The engine pump could not maintain the pressure within the injection chamber, which caused a small 1.1 MPa pressure drop.

This succession of tests reveals the complex HM behavior of the fault with different pressures needed to trigger slip along the fault (STR1 versus STR3), different slip behavior under similar pressure conditions (STR2 versus STR3), and no correlation between the fluid pressure triggering the displacements and the displacement rates.

4. Numerical Simulation of SRT1

We investigated the coupled HM effects during fault reactivation using the TOUGH-FLAC geomechanical numerical simulator. The TOUGH-FLAC simulator (Rutqvist, 2011, 2017) is based on linking the TOUGH2 multiphase flow and heat transport simulator (Pruess et al., 2012) with the FLAC3D geomechanical simulator (Itasca, 2011). In this approach, TOUGH2 (Pruess et al., 2012) is used for solving multiphase flow and heat

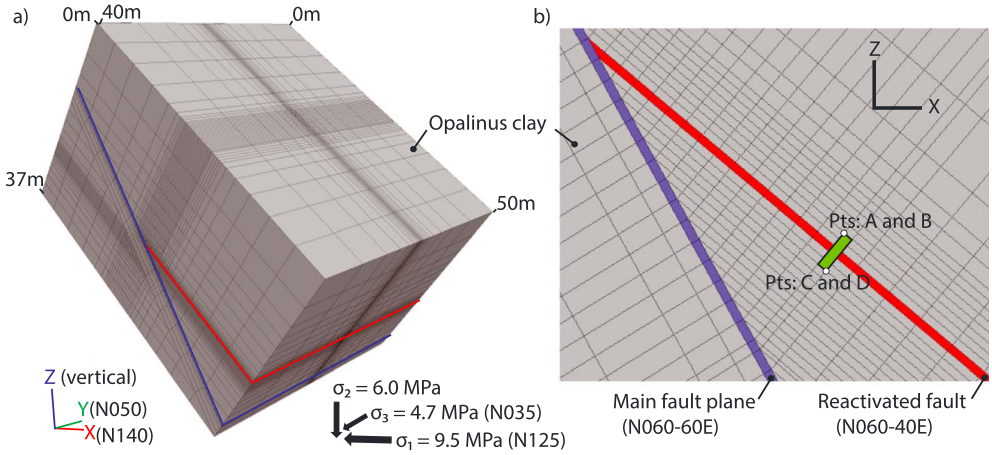

Figure 3. (a) 3D numerical model. (b) Injection chamber intersected by the reactivated fault. The relative displacements are calculated from the displacement of the centers of upper (between points A and B) and lower (between points C and D) boundaries of the injection chamber.

transport equations, whereas FLAC3D (Itasca, 2011) is used for solving geomechanical stress-strain equations. The two codes are sequentially coupled. In a TOUGH-FLAC simulation, the calculation is stepped forward in time with the transient multiphase fluid flow analysis in TOUGH2, and at each time step or at the TOUGH2 Newton iteration level, a quasistatic mechanical analysis is conducted with FLAC3D to calculate stress-induced changes in porosity and intrinsic permeability.

We focus our work on reproducing the fault HM behavior described previously. During these tests, the in situ temperature at the location of the injection did not vary so we ignore thermal effects. The 3D numerical model (60 m × 40 m × 55 m) represents the reactivated and the main fault plane embedded in an anisotropic elastic medium to account for the anisotropic elastic modulus related to the presence of bedding planes (Figure 3a). The injection chamber is located at the center of the model and is represented by solid elements with a cubic shape having a 100% porosity, 10^{-7} m^2 permeability, and the same elastic properties as the surrounding rock. The distance between the upper and lower boundaries of the injection chamber correspond to the distance between the upper and lower rings of the extensometer. The injection chamber is intersected at its center by one fault 0.1 m thick with strike N060° and dipping 40°E. Control points located inside the simulated injection chamber allow calculating the relative displacements of the centers of the upper and lower boundaries of the injection chamber during injection and comparing them with the HPPP measurements (Figure 3b). Stresses following the lithostatic gradients are applied on all the boundaries, and permeable flow boundaries are imposed. A strike-slip stress regime is applied to simulate displacements having the same direction as those monitored during the first rupture (Ev.1) with σ_1 = 9.4 MPa oriented N125°, σ_2 = 6.0 MPa vertical, and σ_3 = 4.7 MPa oriented N035° (Jeanne et al., 2017). The paleostress regime that generated the Main Fault is not accurately known, but the strike-slip regime adopted here appears to be relatively consistent with paleostress estimations from fault planes striations (Nussbaum et al., 2011). The Main Fault was indeed initiated as a shear fault-bend fold in the early stage of the Late Miocene Jura NNW thrusting and then passively steepened during late propagation of the Alpine foreland.

Fluid pressure increase is imposed in the injection chamber at the beginning of each pressure step (black curve on Figure 2a), then pressure is allowed to vary during the pressure step to simulate pressure drop related to leakage (blue curve on Figure 2b). When the failure criterion is reached in one mesh element, plastic deformation occurs, and stresses are transferred to the surrounding elements composing the thin fault layer. This may or may not trigger rupture depending on the stresses acting on these elements and on the pressure fluid variations.

When failure occurs, the simulation time step is automatically adapted between 0.025 s and 0.1 s in order to adequately solve the mass and energy balance equations that describe fluid flow in the system and to solve the geomechanics subproblem. At the same time, the displacements of the grid points associated with reactivated fault elements are calculated, and a slip velocity is estimated.

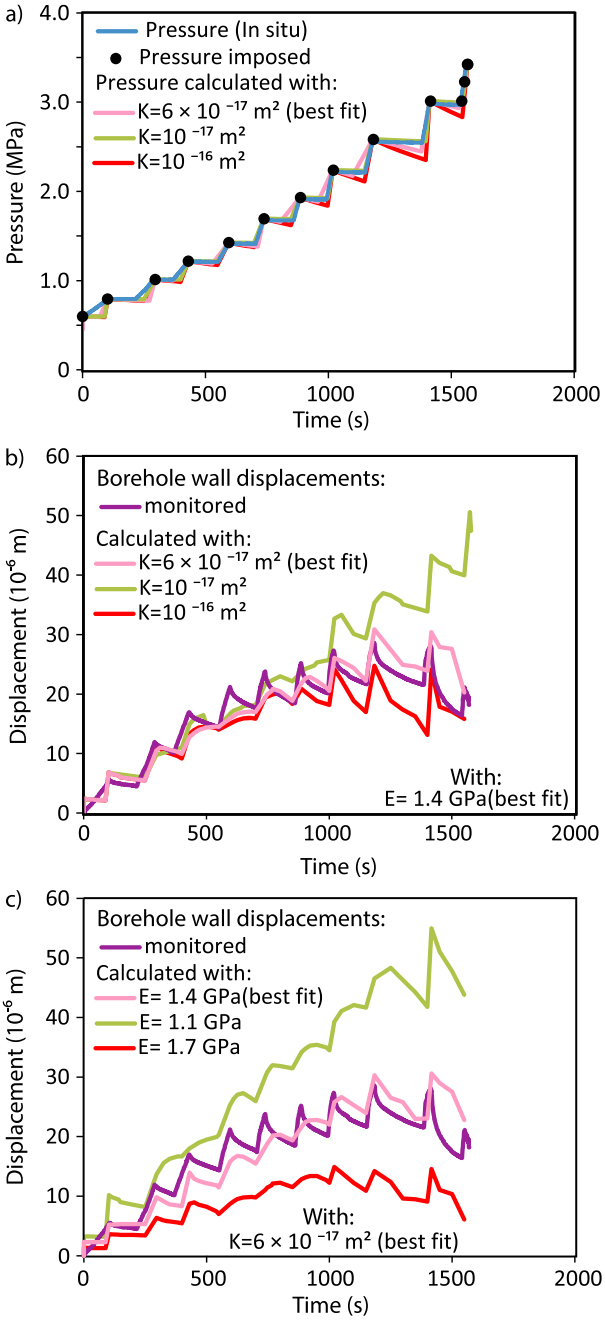

Figure 4. Calibration of the initial HM properties (Young's modulus and permeability) by fitting the simulated and monitoring (a) fluid pressure within the injection chamber and (b and c) the borehole wall displacements.

4.1. Calibration of the Initial Elastic and Hydraulic Properties From SRT1

We first estimate the initial HM properties of the tested interval by reproducing the pressure and the relative borehole wall displacements monitored during SRT1 before Ev.1 (Figure 4). From 0 to 1,000 s (below 2.0 MPa), displacements depend mostly on the mechanical properties (Figures 4b and 4c), and so this part of the curve is used to estimate the Young's modulus (Figure 4c). Then, at higher pressure (from 1,000 to 1,570 s), the fracture permeability has a significant role on the displacement (Figure 4b). So by reproducing both the pressure evolution in the injection chamber (Figure 4a) and the displacement from 1,000 to 1,570 s (Figure 4b), it is possible to estimate the permeability. The best fit, chosen by eye, is found with an initial permeability of 6×10^{-17} m^2 and a Young's modulus of 1.0 GPa for the reactivated fault. A permeability of 10^{-17} m^2 and a Young's modulus of 0.4 GPa and 1.4 GPa normal and parallel to the laminar structure of the claystone for the surrounding rock mass are used for the rock mass (a sensitivity analysis to these mechanical properties is shown in Jeanne et al., 2017). During injection, the fracture permeability evolves due to changes in effective stress. These variations depend on the fracture normal stiffness k_n. Here k_n is equal to 10 GPa/m, which in our continuum model corresponds to a fracture element of 1 GPa Young's modulus divided by a 0.1 m fracture thickness. Very close to the injection chamber, the permeability evolves from 6×10^{-17} to 7.1×10^{-17} m^2 just before Ev.1. Farther away, variations in permeability are negligible (Figures 5k and 5m). The Biot coefficient is 0.7 and the initial rock and fracture porosity is 0.12 (Bossart & Thury, 2008). The main fault (in blue on Figure 3) has the same initial HM properties than the reactivated fault (in red on Figure 3), but in our model, we find that the main fault properties have no influence on the displacement and pressure variation monitored in the injection chamber.

4.2. HM Behavior Simulated Using a Rate Frictional Law and a Rate and State Permeability Law: Best Fit

After calibrating the initial elastic and hydraulic properties, we try to reproduce the fault HM behavior during reactivation. The simulation of dynamic fault rupture propagation and the fully couple HM process using a large numerical grid with variable grid size is very time consuming and requires significant computational power. For simplification, here we used a Mohr-Coulomb elastoplastic model with a rate frictional law linked with a rate and state permeability law (equation ((11))) during a quasistatic mechanical simulation. The parameters used in Simulation 1 (our best fit) are: $(a - b) = -0.0041$, $D_c = 1 \times 10^{-9}$ m, $V_0 = 1 \times 10^{-12}$ m s^{-1}, and $\varepsilon = 5 \times 10^{-4}$. Figures 4a and 4b show the calculated and measured displacement and pressure variations obtained just before, during, and after events 1 and 2 at the end of SRT1. We reproduce the general fault HM behavior with a sharp pressure drop associated with the sudden and large displacement (gray zones in Figure 4) and followed by a pressure stabilization in the injection chamber associated with small and slow displacements of the borehole walls.

To better understand this behavior, we show the evolution of k, μ, and V at four control points within the rupture area estimated to be ≈0.7 m^2 (CP1 to CP4; Figures 5c to 5j) and the evolution of k, μ, P_f, and σ'_n at two control points outside the rupture area (CP5 and CP6; Figures 5k to 5n). We also show several snapshots of these parameters (P_f, k, and μ) within the reactivated fault and with the location of the six control points at 3 s (Figures 6a to 6c) and 130 s (Figures 6d to 5f) after the first rupture (Ev.1).

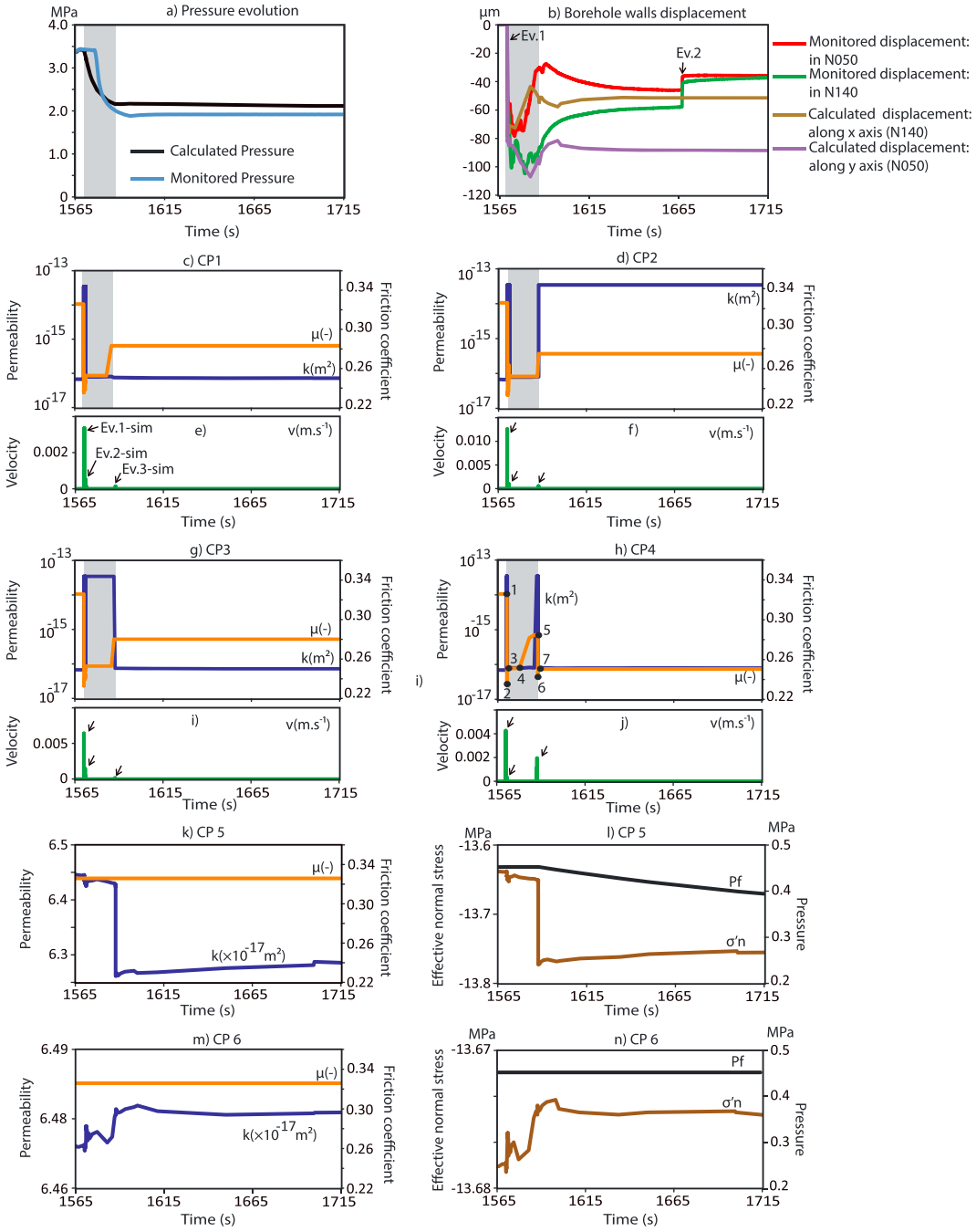

Figure 5. Results of Simulation 1 (Best Fit) with (a) the pressure evolution within the injection chamber, (b) the displacements of the borehole wall with the two monitored events Ev.1 and Ev.2, (c, d g, and h) evolution of the coefficient of friction (μ) and permeability (k), and (e, f, h, and i) slip velocity (V; the three black arrows indicate three rupture events: Ev.1-sim, Ev.2-sim, and Ev.3-sim) of the induced event at four control points located within the rupture area. Evolution of μ, k, P_f, and effective normal stress (σ'_n) at control points located outside the rupture area, (CP5: m and n) ahead of and (CP6: k and l) behind the rupture propagation. The gray area and the black arrows highlight the period during which the pressure evolves in the injection chamber and the slip events along the fault.

4.2.1. Fault HM Behavior Within the Rupture Area

In the rupture area, the HM behavior of the fault during reactivation can be divided into four main phases:

1. From points 1 to 2 (Figure 5h), we observe a first event (Ev.1_sim; Figure 5e) characterized by a velocity weakening behavior (μ drops from 0.32 to 0.23), a large displacement of the borehole walls, a high slip

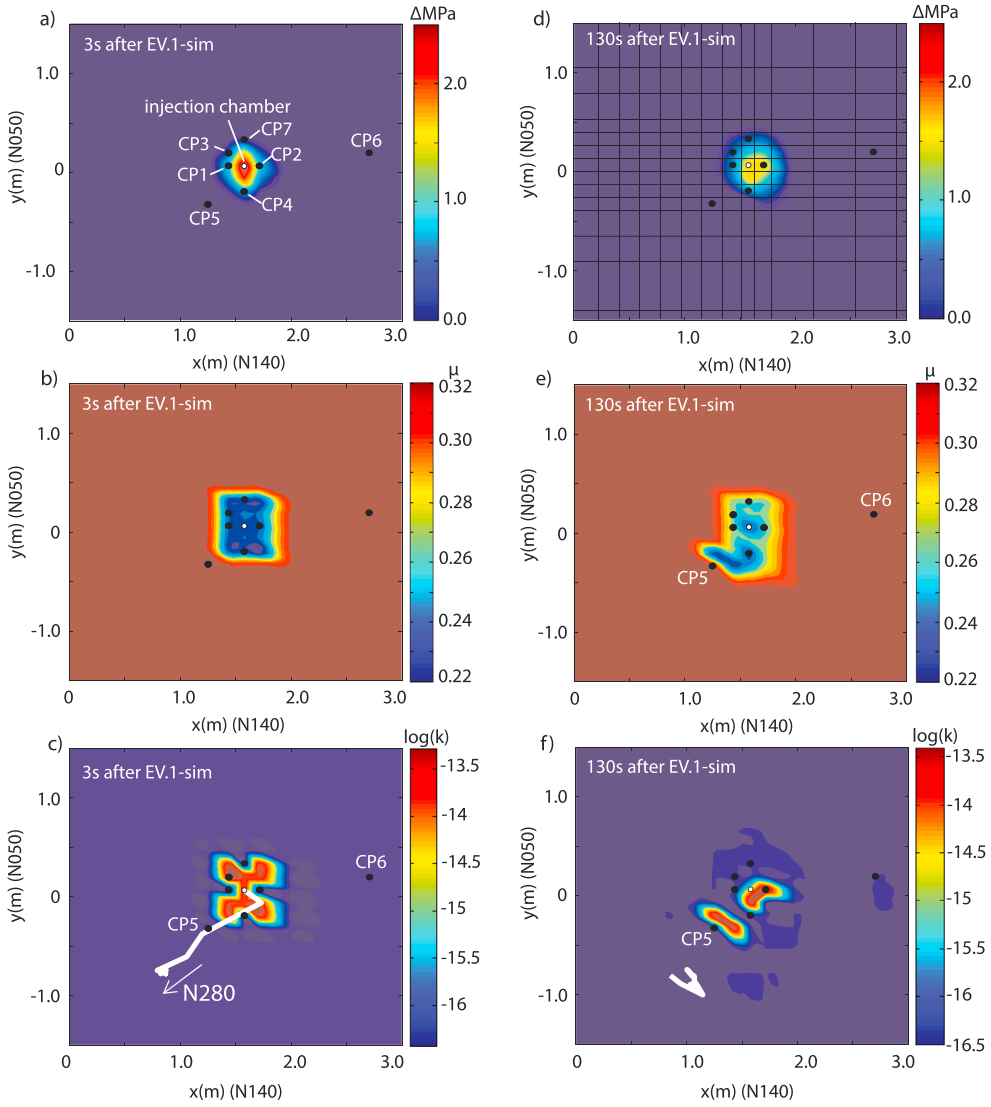

Figure 6. Snapshots showing the spatial distribution of k, μ, and P_f along the reactivated fracture at (a–c) 3 s and (d–f) 130 s, after the main first event (Ev.1_sim), respectively. The white lines represent the borehole displacement monitored during (c) 3 s and (f) 127 s after Ev.1 (not to scale; displacements have been increased a factor of 1,000 times to be seen), and in Figure 6d, the black lines show the mesh.

velocity ($V \approx 0.012$ m s^{-1}), and a strong increase in k up to three orders of magnitude (k from 6×10^{-17} to 3.5×10^{-14} m^2) occurring over the entire rupture area.

2. From points 2 to 3 (Figure 5h), a few tenths of a second later a slip hardening behavior is observed (Ev.2_sim; Figure 5e). It is characterized by smaller displacements of the borehole walls, a lower slip velocity ($V \approx 0.001$ m s^{-1}), and a small increase in μ (from 0.23 to 0.25) over the entire rupture area. This event either destroys (Figures 5c, 5d, and 5h) or preserves (Figure 5g) the permeability.

Three seconds after the main first rupture, the calculated rupture area is larger than the pressurized zone (Figures 6a and 6b), and within the rupture area the changes in permeability are quite heterogeneous (Figure 6c).

1. Then, from points 3 to 5 (Figure 5h), there is a 15 s long pressure diffusion period from the injection chamber into the reactivated fault (gray zone in Figure 5a). This diffusion causes some parts of the fault to fail, but a hardening frictional behavior is observed (point 4 in Figure 5h, where μ increases from 0.25 to 0.28), which prevents unstable slip to propagate. Only small and slow displacements are calculated during this phase (Figure 5b).

Table 1
Parameters Tested During the Sensitivity Analyses

	c	D_c (m)	V_0 (m s^{-1})	ε
Simulation 1 (best fit)	−0.004	1.00E−09	1.00E−12	5.00E−04
Simulation 2	−0.004	1.00E−09	1.00E−12	4.00E−04
Simulation 3	−0.0041	1.00E−09	1.00E−12	1.00E−04
Simulation 4	−0.0043	1.00E−09	1.00E−12	1.00E−04

2. From point 5 to the end, the pressure diffusion into the reactivated fault leads to another rupture. At this moment, the spatial distributions of μ and k within the rupture area are heterogeneous, and different behaviors are observed. There is either (i) a velocity hardening behavior associated with a destruction (Figures 5c and 5g) or an increase (Figure 5d) in k or (ii) a velocity weakening behavior leading to a new rupture event (Ev.3-sim; Figure 5g). In this last case, the drop in μ (from 0.28 to 0.24; point 6 in Figure 5h) results in an unstable rupture ($V \approx 0.002$ m s^{-1}; Figure 5j) and a strong increase in k (up to three orders of magnitude), but a few tenths of a second later a slip hardening behavior is one more time observed (μ increases from 0.24 to 0.25; point 7 in Figure 5h), which stops the rupture and causes k to drop (up to three orders of magnitude; point 7 in Figure 5h).

At 130 s after the main first rupture, the pressure has diffused (Figure 6d), the rupture area has extended (Figure 6e), and the distribution of k, μ, and P_f are quite heterogeneous (Figures 6d to 6f).

4.2.2. Fault HM Behavior Outside the Rupture Area

The directions of the horizontal displacements of the borehole walls calculated during the 3 s following the main rupture and during the following 127 s are represented in Figures 6c and 6f by two white lines. Most of the calculated displacements result from the main rupture that propagates into the direction ≈N280° (Figure 6c). The control points CP5 and CP6 are respectively located in front and behind the rupture propagation (Figure 6c), both being outside the rupture area. However, at these two locations, a change in σ'_n is observed acting on the fault due to the stress redistribution associated with the main rupture. In front of the rupture area (at CP5), σ'_n increases (Figure 5l) resulting in a slight decrease in k (from 6.46×10^{-17} to 6.29×10^{-17} m^2; Figure 5k). Inversely, behind the rupture area (at CP6), σ'_n decreases (Figure 5n) resulting in a slight increase in k (from 6.46×10^{-17} to 6.48×10^{-17} m^2; Figure 5m). According to equation (11), the amount of permeability variation is related to the normal stiffness of the fault. It is also interesting to notice that CP5 is located just at the boundary of the rupture area in an area where k (and so the porosity) has strongly increased (Figure 5p) but where the injected pressure fluid pressure has not yet diffused (Figure 6d). This strong increase in porosity has depressurized this part of the rupture area inducing fluid diffusion from the nonreactivated zone toward the rupture area. This phenomenon caused the pressure drop calculated at CP5 (Figure 5h).

4.3. Sensitivity Analysis to the Coefficient of Dilation

Here we vary the coefficient of dilation (ε) to change the amount of leakage from the injection chamber into the reactivate fault (Simulation 2) and to compare with the best fit (Simulation 1). In Simulation 2 the coefficient of dilation (ε) is slightly smaller (Table 1). During the first 15 s following the main rupture, the two simulations show very similar results. However, in Simulation 2 because ε is slightly lower, the increase in permeability is smaller, and the pressure diffusion within the reactivated fault is slower (gray stripe in Figure 7a). This has an important influence on the rupture propagation. In both simulations, a rupture is induced around 1,590 s (Ev3_sim; Figure 7e), but Ev3_sim occurs at a higher fluid pressure in the case of Simulation 2 and is characterized by larger displacements (Figure 7b) and a higher slip velocity (Figure 7e) than in Simulation 1 (best fit). In this case, Ev3_sim destroys k in some part of the fault as observed in simulation 1 (Figures 7g and 7h) but also enhances k in other locations (Figures 7c and 7d). So the fluid pressure keeps diffusing through the fault inducing four other small slip events (black arrows on Figure 7e). Within the injection chamber, the pressure keeps decreasing until a small rupture leads to pressure stabilization around 1,650 s (Figure 7a). This small rupture has destroyed the permeability somewhere within the reactivated area creating several parts where the permeability has been increased but which are not connected (Figures 7k and 7l). This bad connectivity prevents the fluid to diffuse and causes the pressure stabilization in the injection chamber.

4.3. Sensitivity Analysis to $a - b$

In Simulations 3 and 4, we looked at the amount of weakening effect, which is lower in Simulation 3 ($c = -0.0041$) than in Simulation 4 ($c = -0.0043$), on the HM behavior of the reactivated fault. In these two cases, the coefficient of dilation has been lowered to 1×10^{-4} (Table. 1). Both simulations show only

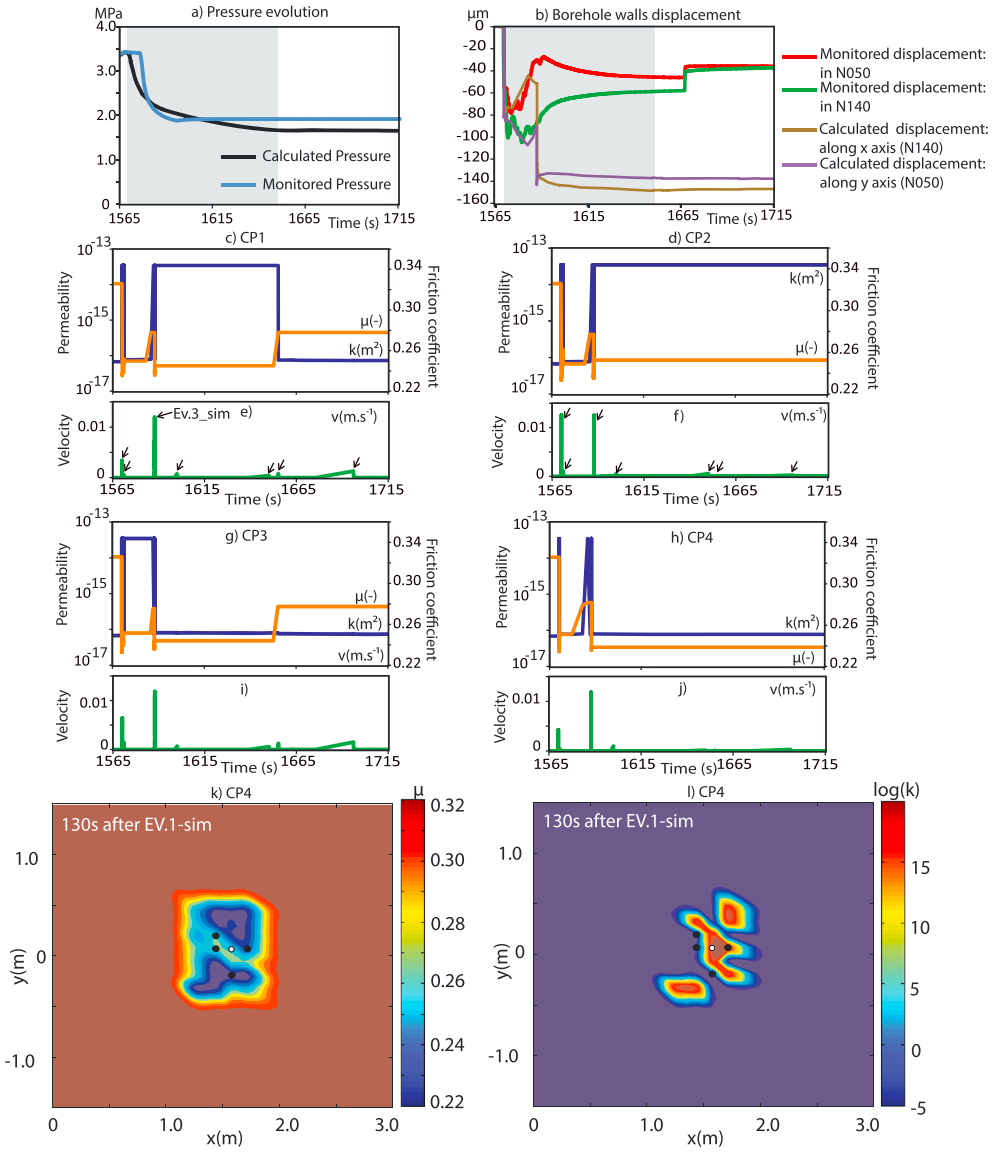

Figure 7. Results of Simulation 2 with (a) the pressure evolution within the injection chamber, (b) the displacements of the borehole wall, (c, d, g, and h) evolution of permeability and coefficient of friction, and (e, f, i, and j) slip velocity at four control points located within the reactivated fault. The gray area and the black arrows highlight the period during which the pressure evolves in the injection chamber and the rupture events along the fault. (k–l) Snapshots showing the spatial distribution of μ and k along the reactivated fracture at 130 s, after the main first event (Ev.1_sim), respectively.

one main rupture with a slip velocity around 0.02 m s^{-1} (Figures 8d and 8h), a rupture area of similar size and almost similar displacement (the associated displacement of the borehole walls are slightly lower in the case of Simulation 3 where the amount of weakening is lower; Figures 8b and 8f). Despite these similarities, the pressure evolutions within the injection chamber are quite different with a very small pressure drop in Simulation 3 (Figure 8a) and a large and continuous pressure drop in Simulation 4 (Figure 8e). This difference is due to the spatial distribution of the changes in k within the rupture areas. In Simulation 4, the part of the fault where k has been enhanced is larger and is connected to the injection chamber (Figure 8j), which allows larger pressure diffusion. Inversely, in Simulation 3, the part of the fault k that has been enhanced is smaller and is not connected to the injection chamber (Figure 8i), which prevents the pressure diffusion. Finally, it is interesting to notice that either small or large pressure diffusion along the reactivated fault do not induce a secondary rupture (Figures 8d and 8h) because in both cases fluid pressure is too small.

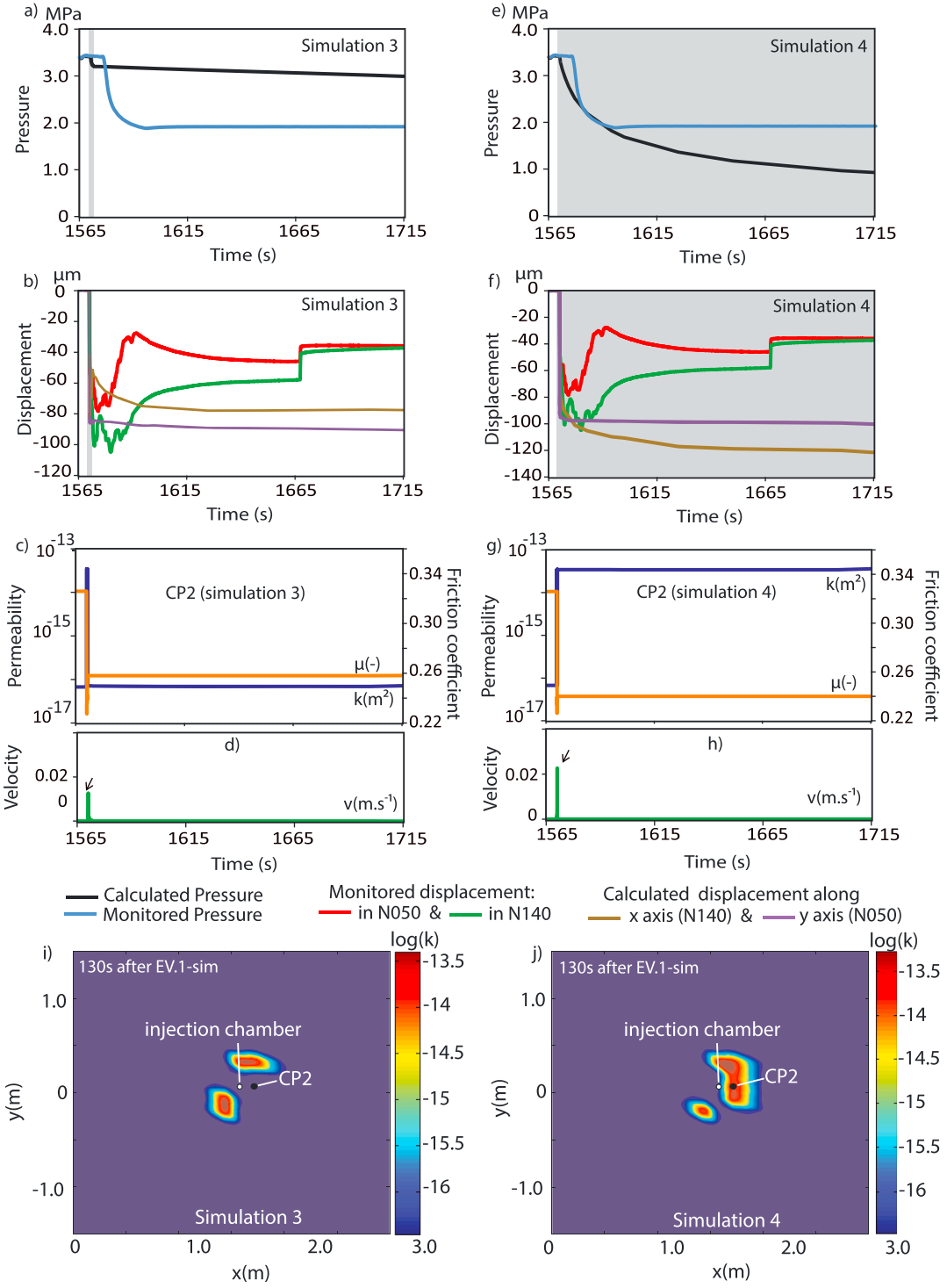

Figure 8. Results of Simulations 3 and 4 with (a, e) the pressure evolution within the injection chamber, (b, f) the displacements of the borehole wall, (c, g) evolution of the coefficient of friction, permeability, and (d, h) slip velocity at one control point (CP2); and snapshots showing the spatial distribution of *k* at (i, j) 130 s, after the main first event (Ev.1_sim), respectively. The gray area and the black arrows highlight the period during which the pressure evolves in the injection chamber and the slip events along the fault.

5. Numerical Simulation of the Entire HM Test: SRT1 to SRT3

In this part, we attempt to reproduce the successive different fault HM behaviors observed during the entire injection test. We used the same modeling approach to simulate the injection history as previously, imposing

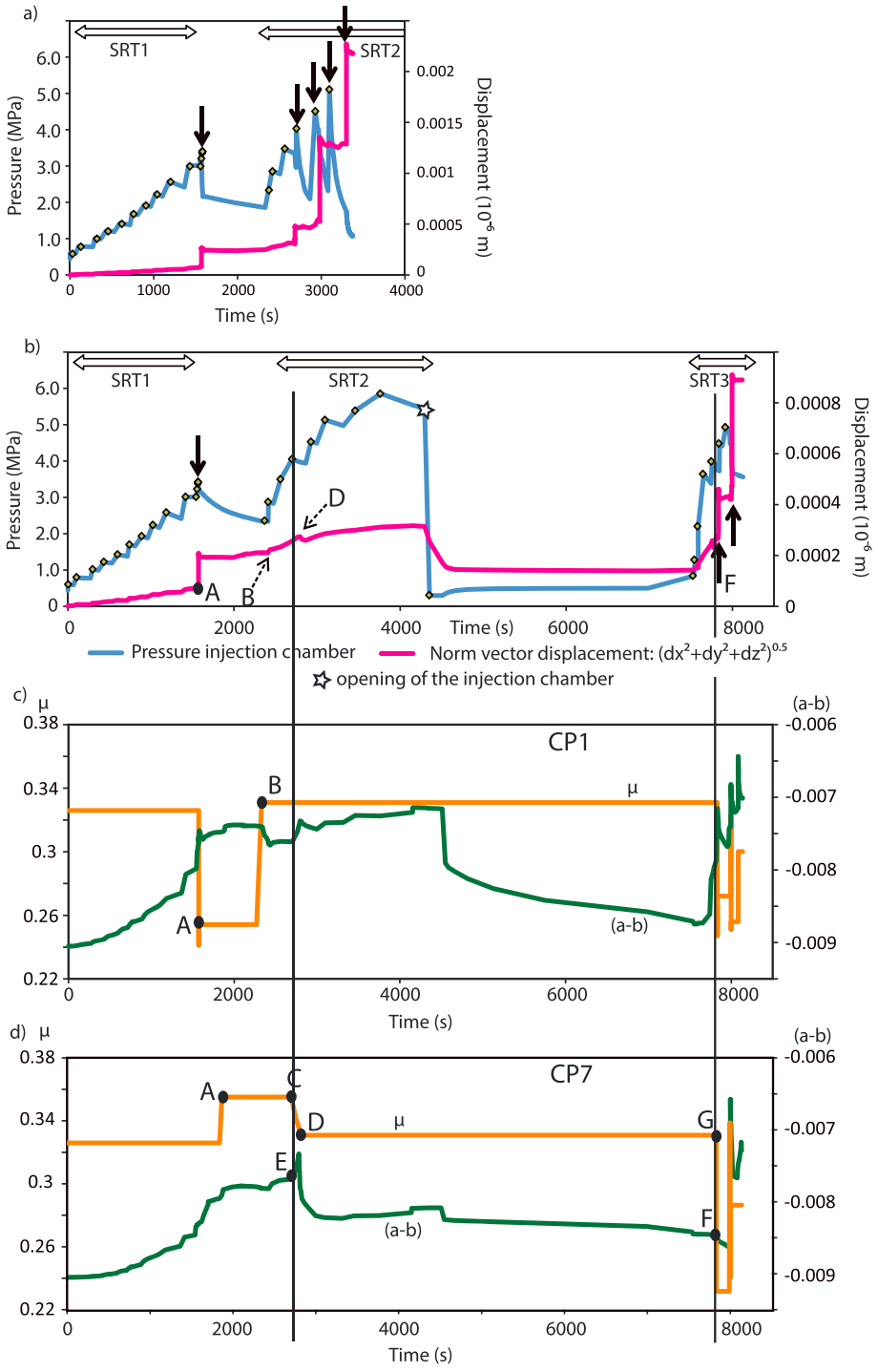

Figure 9. Pressure evolution within the injection chamber and the displacements of the borehole wall calculated from (a) Simulation 5 and (b) Simulation 6. (c, d) The evolution of the constitutive parameter ($a - b$) and μ during Simulation 6 at two control points within the reactivated fault (Cp1 and Cp7; Figure 6a).

the first point of each pressure step (black curves in Figure 2a) and calculating the remaining parts (blue curves in Figure 2a). The diamonds in Figure 9 show when the pressure is imposed.

We first use the same parameters as in STR1 (best fit). The general fault HM behavior that matches during SRT1 is not reproduced for the successive injection tests (Figure 8a). Several large ruptures associated with several large pressure drops are calculated during SRT2 (the four black arrows in Figure 9a), but they are

not measured during the field experiment (Figure 2a). For this reason, the simulation was stopped before the end of the test.

Then, we performed a new simulation (Simulation 5) where the rate-and-state constitutive parameter $(a - b)$ is now considered pressure dependent as suggested by Scruderi and Collettini (2016). For this simulation, we develop equation (12) where an increase in pressure leads to an increase in $(a - b)$ favoring a stable sliding.

$$(a - b) = (a - b)_0 \times (P_{f0}/P_f)^{0.2} \tag{12}$$

These changes in $(a - b)$ influence the coefficient of friction only during changes in slip velocity (equation (6)). Simulation results are shown in Figure 9b. The fault displacements (Figure 2a) during the entire test are reproduced reasonably well: (i) a first large event triggered at 3.3 MPa during STR 1, (ii) no large rupture during STR 2 despite a maximum fluid pressure close to 6.0 MPa, and (iii) finally a large rupture triggered at fluid pressure equal to 3.9 MPa during STR 3. Such a complex HM behavior is due to a combination of several factors:

1. The strengthening due to the pressure increase (equation (12)). Large or small ruptures have resulted in an increase of μ, for example, from 0.32 to 0.35 at point A (Figure 9d) and from an initial value of $\mu = 0.32$ to $\mu = 0.338$ after a series of ruptures (point B; Figure 9c). When rupture nucleates, this strengthening prevents a large drop in μ to occur and stops the rupture propagation (points C to D; Figure 9d).
2. The amount of pressure diffusion into the fault. This is well shown by the two black lines in Figure 9, which highlights two ruptures triggered at the same injection pressure around 4 MPa but occurring at different diffusion times. One of the ruptures occurred during SRT2 and did not propagate, whereas the other one occurred during SRT3 and propagated. This difference is due to the amount of weakening during the slip, which was lower during the first rupture corresponding to a small pressurized area ($a - b \approx -0.0077$; Figure 9d, point E) and higher during the second rupture corresponding to a large pressurized area ($a - b \approx -0.0084$; Figure 9d, point F).
3. The slip history. The phenomenon described previously is also possible because small ruptures that did not propagate during SRT2 have caused a small drop in μ favoring a rupture nucleation at lower fluid pressure during SRT3 (difference between points C and G on Figure 9d).

6. Discussion

6.1. Comparison of Permeability Laws Using SRT1

We tried to reproduce the pressure drop associated with the sudden and large displacement of the borehole walls monitored at the end of SRT 1 using different frictional and permeability laws. Here we compare the results obtained with the rate frictional law and a rate-and-state Permeability Law 3 with the simpler Permeability Laws 1 (equation (7)) and 2 (equation (9)).

In the case of Permeability Law 1, we present three simulation results where the coefficient of friction drops from 0.32 to a residual value of 0.23 when the plastic shear strain reaches a critical value of 10^{-5}, and the initial permeability is enhanced by a fixed factor of 10, 100, or 1,000 where the failure criterion is reached (Figure 10a). In this law, it clearly appears that the main factor controlling the amount of displacement is the factor by which the permeability is enhanced (Figures 10b and 10c). It is directly related to equation ((1)). A strong permeability increase favors the fluid diffusion into the fault that increases the fluid pressure and promotes shear failure.

In case of Permeability Law 2, we only present two simulation results where the coefficient of friction drops from 0.32 to a residual value of 0.24 and 0.22 when the plastic shear strain reaches a critical value of 10^{-5} (Figure 10d). In this case, the drop in the friction coefficient is the main factor controlling the amount of plastic shear strain and the changes in permeability (Figure 10f). However, permeability changes are small; the permeability increases from 6.7×10^{-17} m^2 to $7.1 \pm 0.1 \times 10^{-17}$ m^2 (Figure 10d) and have little influence on the pressure in the injection chamber (Figure 10e). Other simulations were done with a dilation angle (ψ) of the reactivated fault of 5°, 15°, or 25°, but again changes in permeability were negligible, and they did not influence the displacement neither the pressure drop within the injection chamber.

In summary, contrary to the rate frictional law coupled with a rate-and-state permeability law, Permeability Laws 1 and 2 do not consider the possibility that locally along the reactivated fault porosity can be

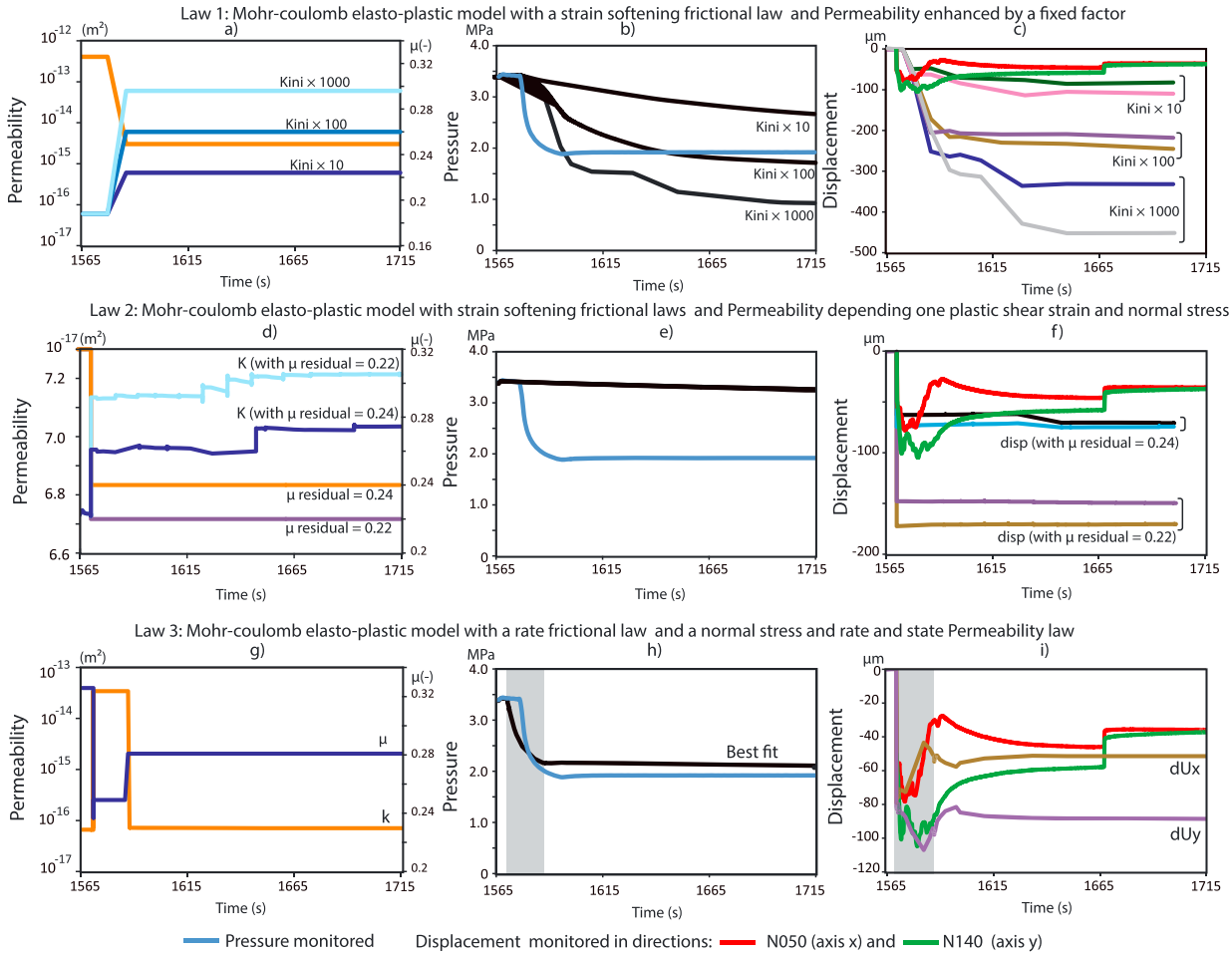

Figure 10. Comparative study between the monitoring and calculated (b, e, h) pressure within the injection chamber and (c, f, i) displacement of the borehole walls using the frictional and Permeability Laws (a) 1, (d) 2, and (g) 3.

destroyed. So Laws 1 and 2 fail to reproduce the pressure stabilization a few seconds after the main rupture and the secondary event observed while the pressure is constant within the injection room.

6.2. Rupture and Fluid Diffusion

In our simulations, the fluid overpressure triggers a slip that is always characterized by a drop in μ associated with a strong increase in permeability both occurring over the entire rupture area. The rupture propagates farther than the pressurized area and ends when the slip velocity becomes low enough to cause an increase in μ. This decrease in slip velocity can also result in a porosity compaction destroying the permeability. The consequence is that the simulated rupture area is very heterogeneous with strong contrasts in μ (0.22 to 0.32) and permeability (up to three orders of magnitude). Our results show that for rupture patches of almost similar sizes, the fluid overpressure diffusion can be small to large depending on the connectivity between the parts of the rupture areas where the permeability has been increased. Secondary ruptures are triggered when the diffusion is not too low to prevent the fluid to diffuse and not too high allowing pressure to effectively diffuse.

6.3. Consequences for Induced Seismicity

This injection test highlights a complex HM behavior of the reactivated fault with different pressure increases needed to trigger slip along the fault (STR1 versus STR3) and different slip behavior under similar pressure conditions (STR2 vs STR3). Our numerical analyses of this test reveal the importance of the following:

1. The slip history, which influences the distribution and the variability of μ along the fault;

2. The pressure loading, which influences the pressure diffusion, and thus the size of the pressurized area and the magnitude of the fluid overpressure; and
3. The rate-and-state parameter ($a - b$) that depends on the fluid pressure, which influences in our case the amount of weakening.

We also show that the rupture area is much larger than the pressurized area. So based on all these observations and under these conditions, we can argue that once a first rupture has propagated, it is easier for the following rupture (i) to nucleate at the pressure front where μ has dropped and (ii) to propagate because of the lower fluid pressure that causes a lower strengthening behavior. Inversely, in the overpressurized zone, both the possible increase in μ and the stress drop associated to the first rupture make it harder for a second slip to nucleate, and if nucleation occurs, the high fluid pressure will cause a strong strengthening behavior preventing the rupture to propagate.

Finally, our results suggest that it is not straightforward to relate the seismic moment of a single seismic event to a change in fault permeability because there are significant differences between the dimensions of enhanced permeability patches and the potentially seismic rupture areas (calculated using rate frictional law coupled with a rate-and-state permeability law constitutive law). On the other hand, the propagation of seismic events can be used to estimate the overpressure diffusion. However, we also show that observing the eventual temporal-spatial propagation of seismic events associated with the pressure diffusion does not mean that a permanent hydraulic pathway has been created between the main seismic event and the following rupture. The absence of pressure variation within the injection chamber during the second rupture illustrates this point.

7. Conclusion

Pore fluid diffusion along faults is one of the primary mechanisms of induced fault geomechanical instability. Fault slip is coupled with fluid flow, and assessing (i) whether seismic or aseismic slip should result from a fluid injection and (ii) how the fault sealing capacity is affected is a challenge. To better understand this processes, a series of field stimulation tests where multiple fault slips were triggered by fluid pressurization in a borehole were performed, and results were analyzed through numerical simulations using different frictional and permeability laws. Our main findings from the numerical modeling are as follows:

1. A rate frictional law and a rate-and-state permeability law allow reproducing one test, but it appears that the rate constitutive parameters ($a - b$) must be updated to reproduce the complex HM behavior observed during the successive injection tests.
2. Changes in permeability within the reactivated area are quite heterogeneous (up to three orders of magnitudes).
3. The connectivity between these zones of enhanced permeability plays a tremendous role on the fluid diffusivity.
4. Depending on HM history, almost similar ruptures can create a pathway for fluid to diffuse or not.
5. A too high or too low diffusivity created by the main rupture prevents secondary event to occur whereas "intermediate" diffusivity favors the nucleation of a secondary rupture associated with the fluid diffusion.
6. A succession of ruptures does not necessarily create a continuous hydraulic pathway as observed during the injection experiment.
7. Small permeability variations occur in front and behind the rupture propagation associated with the stress redistribution.

Acknowledgments
The authors are deeply grateful to the four partners of the Mont Terri Project that contributed to the funding of the FS experiment: the Swiss Federal Office of Topography (Swisstopo), the Swiss Federal Nuclear Safety Inspectorate (ENSI), the Japanese Atomic Energy Agency (JAEA), and the U.S. Department of Energy. The Mont Terri Project is an international research project for the hydrogeological, geochemical, and geotechnical characterizations of a clay formation (Opalinus Clay). Funding for Berkeley Lab's analysis of the FS data as described in this study was provided by the Assistant Secretary for Fossil Energy as part of the Core Carbon Storage and Monitoring Research (CCSMR) and National Risk Assessment Partnership (NRAP) programs of the U.S. Department of Energy under contract DEAC02-05CH11231. We are also grateful to the journal Editor Yehuda Ben-Zion, Dave Healy, and another anonymous person who reviewed this paper. Experimental data are available in the supporting information.

References

Amontons, G. (1699). De la resistance causée dans les Machines, tant par les frottemens des parties qui les composent, que par roideur des cordes qu'on y employe, & la maniere de calculer l'un & l'autre. Mémoires de l'Académie royale des sciences. In *Histoire de l'Académie Royale des Sciences* (pp. 206–222).

Bandis, S. C., Lumsden, A. C., & Barton, N. R. (1983). Fundamentals of rock joint deformation. *International Journal of Rock Mechanics and Mining Science and Geomechanics Abstracts*, *20*(6), 249–268. https://doi.org/10.1016/0148-9062(83)90595-8

Bossart, P., & Thury, M. (2008). *Mont Terri Rock Laboratory. Project, programme 1996 to 2007 and results*. *Reports of the Swiss Geological Survey* (Vol. 3, 445 pp.). Wabern, Switzerland Swisstopo, Seftigenstrasse.

Carpenter, B. M., Scuderi, M. M., Collettini, C., & Marone, C. (2014). Frictional heterogeneities on carbonate-bearing normal faults: Insights from the Monte Maggio Fault, Italy. *Journal of Geophysical Research: Solid Earth*, *119*, 9062–9076. https://doi.org/10.1002/2014JB011337

Coulomb, C. A. (1773). Application des règles de maxima et minima à quelques problèmes de statique relatifs a l'Architecture. In *MeÂmoires de MatheÂmatique et de Physique, Acad. Roy. Sci. Mem. Math. Phys.* (Vol. 7, pp. 343–528). Paris: Imp. R. Acad. Sci.

Dieterich, J. H. (1978). Time-dependent friction and the mechanics of stick-slip. *Pure and Applied Geophysics*, *116*(4-5), 790–806. https://doi.org/10.1007/BF00876539

Dieterich, J. H. (1979). Modeling of rock friction, 1. Experimental results and constitutive equations. *Journal of Geophysical Research*, *8*, 2161–2168. https://doi.org/10.1029/JB084iB05p02161

Giardini, D. (2009). Geothermal quake risks must be faced. *Nature*, *462*(7275), 848–849. https://doi.org/10.1038/462848a

Guglielmi, Y., Cappa, F., Avouac, J., Henry, P., & Elsworth, D. (2015). Seismicity triggered by fluid injection-induced aseismic slip. *Science*, *348*(6240), 1224–1226. https://doi.org/10.1126/science.aab0476

Guglielmi, Y., Cappa, F., Lançon, H., Janowczyk, J. B., Rutqvist, J., Tsang, C. F., & Wang, J. S. Y. (2013). ISRM suggested method for step-rate injection method for fracture in-situ properties (SIMFIP): Using a 3-components borehole deformation sensor. *Rock Mechanics and Rock Engineering*, *47*(1), 303–311. https://doi.org/10.1007/s00603-013-0517-1

Guglielmi, Y., Elsworth, D., Cappa, F., Henry, P., Gout, C., Dick, P., & Durand, J. (2015). In situ observations on the coupling between hydraulic diffusivity and displacements during fault reactivation in shales. *Journal of Geophysical Research: Solid Earth*, *120*, 7729–7748. https://doi.org/10.1002/2015JB012158

Gutierrez, M., Oino, L. E., & Nygard, R. (2000). Stress-Dependent Permeability of a De-Mineralised Fracture in Shale. *Marine and Petroleum Geology*, *17*, 895–907.

Hand, E. (2014). Injection wells blamed in Oklahoma earthquakes. *Science*, *345*(6192), 13–14.

Hsiung, S. M., Chowdhury, A. H., & Nataraja, M. S. (2005). Numerical simulation of thermal-mechanical processes observed at the Drift-Scale Heater Test at Yucca Mountain, Nevada, USA. *International Journal of Rock Mechanics and Mining Sciences*, *42*(5–6), 652–666.

Hubbert, M. K., & Rubey, W. W. (1959). Role of fluid pressure in mechanics of overthrust faulting I. Mechanics of fluid-filled porous solids and its application to overthrust faulting. *Geological Society of America Bulletin*, *70*(2), 115–166.

Itasca (2011). *FLAC3D V5.0. Fast Lagrangian analysis of continua in 3 dimensions, user's guide*. Minneapolis, MN: Itasca Consulting Group.

Jeanne, P., Guglielmi, Y., Rutqvist, J., Nussbaum, C., & Birkholzer, J. (2017). Field characterization of elastic properties across a fault zone reactivated by fluid injection. *Journal of Geophysical Research: Solid Earth*, *122*, 6583–6598. https://doi.org/10.1002/2017JB014384

Jeanne, P., Rutqvist, J., Hartline, C., Garcia, J., Dobson, P. F., & Walters, M. (2014). Reservoir structure and properties from geomechanical modeling and microseismicity analyses associated with an enhanced geothermal system at The Geysers, California. *Geothermics*, *51*, 460–469. https://doi.org/10.1016/j.geothermics.2014.02.003

Marone, C. (1998). Laboratory-derived friction laws and their application to seismic faulting. *Annual Review of Earth and Planetary Sciences*, *26*(1), 643–696. https://doi.org/10.1146/annurev.earth.26.1.643

Marone, C., Raleigh, C. B., & Scholz, C. H. (1990). Frictional behavior and constitutive modeling of simulated fault gouge. *Journal of Geophysical Research*, *95*(B5), 7007–7025. https://doi.org/10.1029/JB095iB05p07007

Nussbaum, C., Amann, F., Aubourg, C., & Bossart, P. (2011). Analysis of tectonic structures and excavation induced fractures in the Opalinus Clay, Mont Terri underground rock laboratory (Switzerland). *Swiss Journal of Geosciences*, *104*, 187–210.

Pine, R. J., & Batchelor, A. S. (1984). Downward migration of shearing in jointed rock during hydraulic injections. *International Journal of Rock Mechanics and Mining Sciences*, *21*(5), 249–263. https://doi.org/10.1016/0148-9062(84)92681-0

Pruess, K., Oldenburg, C. M., & Moridis, G. (2012). *TOUGH2 user's guide, version 2.1, LBNL-43134(revised)*. Berkeley, CA: Lawrence Berkeley National Laboratory.

Rabinowicz, E. (1958). The intrinsic variables affecting the stick-slip process. *Proceedings of the Physical Society of London*, *71*(4), 668–675. https://doi.org/10.1088/0370-1328/71/4/316

Rinaldi, A. P., Rutqvist, J., & Cappa, F. (2014). Geomechanical effects on CO_2 leakage through fault zones during large-scale underground injection. *International Journal of Greenhouse Gas Control*, *20*, 117–131. https://doi.org/10.1016/j.ijggc.2013.11.001

Rinaldi, A. P., Rutqvist, J., Sonnenthal, E. L., & Cladouhos, T. T. (2015). Coupled THM modeling of hydroshearing stimulation in tight fractured volcanic rock. *Transport in Porous Media*, *108*(1), 131–150. https://doi.org/10.1007/s11242-014-0296-5

Ruina, A. L. (1983). Slip instability and state variable friction laws. *Journal of Geophysical Research*, *88*(B12), 10,359–10,370. https://doi.org/10.1029/JB088iB12p10359

Rutqvist, J. (2011). Status of the TOUGH-FLAC simulator and recent applications related to coupled fluid flow and crustal deformations. *Computers & Geosciences*, *37*(6), 739–750. https://doi.org/10.1016/j.cageo.2010.08.006

Rutqvist, J. (2017). An overview of TOUGH-based geomechanics models. *Computers & Geosciences*, *108*, 56–63. https://doi.org/10.1016/j.cageo.2016.09.007

Rutqvist, J., Rinaldi, A. P., Cappa, F., Jeanne, P., Mazzoldi, A., Urpi, L., et al. (2016). Fault activation and induced seismicity in geologic carbon storage—Lessons learned from recent modeling studies. *Journal of Rock Mechanics and Geotechnical Engineering*, *8*(6), 789–804. https://doi.org/10.1016/j.jrmge.2016.09.001

Rutqvist, J., & Stephansson, O. (2003). The role of hydromechanical coupling in fractured rock engineering. *Hydrogeology Journal*, *11*(1), 7–40. https://doi.org/10.1007/s10040-002-0241-5

Scholz, C. (1998). Earthquakes and friction laws. *Nature*, *391*(6662), 37–42. https://doi.org/10.1038/34097

Scruderi, M. M., & Collettini, C. (2016). The role of fluid pressure in induced vs. triggered seismicity: Insights from rock deformation experiments on carbonates. *Scientific Reports*, *6*, 24852. https://doi.org/10.1038/srep24852

Segall, P., & Rice, J. R. (1995). Dilatancy, compaction, and slip instability of a fluid-infiltrated fault. *Journal of Geophysical Research*, *100*(B11), 22,155–22,171. https://doi.org/10.1029/95JB02403

Sleep, N., & Blanpied, M. (1992). Creep, compaction and the weak rheology of major faults. *Nature*, *359*(6397), 687–692. https://doi.org/10.1038/359687a0

Tagliabue, J. (2013). *Parts of low country are now quake country* (p. A6). New York Times.

Terzaghi, K. (1923). Die Berechnung der Durchlassigkeitziffer des Tones aus dem Verlauf der hydrodynamischen Spannungserscheinungen. *Akad Wissensch Wien Sitzungsber Mathnaturwissensch Klasse IIa*, *142*(3/4), 125–138.

Townend, J., & Zoback, M. D. (2001). How faulting keeps the crust strong. *Geology*, *28*, 399–402.

Zoback, M. D., & Gorelick, S. M. (2012). Earthquake triggering and large-scale geologic storage of carbon dioxide. *Proceedings of the National Academy of Sciences of the United States of America*, *109*(26), 10,164–10,168. https://doi.org/10.1073/pnas.1202473109